Biochemical Pharmacology 80 (2010) 990–999

Contents lists available at ScienceDirect

Biochemical Pharmacology

journal homepage: www.elsevier.com/locate/biochempharm

Temperature dependent photolabeling of the human angiotensin II type 1 receptor reveals insights into its conformational landscape and its activation mechanism

Jason Arsenault, Jérôme Cabana, Dany Fillion, Richard Leduc, Gaétan Guillemette, Pierre Lavigne *, Emanuel Escher *

Département de Pharmacologie, Faculté de médecine et des sciences de la santé, Université de Sherbrooke, Sherbrooke, Québec, Canada J1H 5N4

ARTICLE INFO

Article history:
Received 14 April 2010
Accepted 7 June 2010

Keywords:
GPCR
Photolabeling
Molecular modeling
Constitutive activity
Angiotensin II

ABSTRACT

We present a photoaffinity labeling study of the human Angiotensin II (AngII) type 1 receptor (hAT_1) and a constitutively active mutant (CAM) N111G hAT_1 at multiple temperatures using a p-benzoyl-L-phenylalanine (Bpa) containing AngII analogue ^{125}I-[Sar^1, Bpa^8] AngII and the Methionine Proximity Approach (MPA). By introducing Met residues, which react selectively with Bpa, by mutagenesis in hAT_1 and its CAM, we were able to identify the position of residues that surround the Bpa moiety in the receptor–ligand complexes. Here we refined this characterization by controlling and varying (from −20 to 50 °C) the temperature at which the photolabeling was carried out. The hAT_1 Met mutant, as well as CAM double mutant, photolabeled receptors were digested with CNBr and the fragmentation patterns were quantified by radioactive and densitometric analysis. Many important and significant changes in the fragmentation patterns were observed as function of both the temperature of photolysis and the context of constitutive activation. The ligand–receptor complex was increasingly flexible as temperature was increased, i.e. that the Bpa moiety could more easily label increasingly distant residues. These fragmentation patterns were converted into distance constraints that were included into a simulated annealing protocol in order to explore the extent of these conformational changes. In the context of constitutive activation, the 6th transmembrane domain (TM6) was found to exhibit a relative outward movement while TM2 and 5 were found to move closer to the ligand binding site. TM3 showed a slight displacement.

1. Introduction

The relationship between structures of protein ligand complexes and biological activity is of crucial importance to rational drug design. Amongst highly sought after drug targets are the important family of G protein coupled receptors (GPCR). However the structural characterization of GPCR–ligand complexes still represents an extremely daunting task, even though recent advances in X-ray crystallography have permitted high resolution structures of some of these receptors [1–3]. Besides their transmembrane association, the innate conformational dynamics of GPCRs that allows for the existence of diverse pathways of activation through multiple interactions contributes to the difficulty of their structural characterization [4–9]. Newer theories are taking into account the more dynamic nature of protein–ligand interaction, instead of unique static conformations [4,9,10]. Hence, approaches complementary to X-ray crystallography that allow for the characterization of the dynamic nature of the structures of GPCR are thus necessary to investigate this class of membrane proteins.

The human angiotensin II type 1 receptor (hAT_1) has been highly scrutinized for many decades. The hormone angiotensin II (AngII) is responsible for the maintenance of vascular tonus, aldosterone secretion and electrolyte homeostasis [11]. The hAT_1 receptor canonically signals through the $G_{q/11}$/phospholypase C/Inositol triphosphate pathway. Further studies have found other interacting G proteins, such as $G_{i/o}$ and $G_{12/13}$ as well as G protein independent pathways depending on cellular context [12]. This further highlights the conformationally adaptive nature of hAT_1 and GPCRs in general, widening the gap away from the original static "lock and key" mechanism [13].

The hAT_1 receptor is constitutively active once the residue Asn 111 (3.35) is mutated to glycine [14]. This constitutively active mutant (CAM) has given much insight into structural mechanisms

* Corresponding authors at: 3001 12e Ave. N., Sherbrooke, Québec, Canada J1H 5N4. Tel.: +1 819 820 6868 15462 (P. Lavigne).
E-mail addresses: Pierre.Lavigne@usherbrooke.ca (P. Lavigne), Emanuel.Escher@usherbrooke.ca (E. Escher).

0006-2952/$ – see front matter © 2010 Elsevier Inc. All rights reserved.
doi:10.1016/j.bcp.2010.06.004

of constitutive activity [14–17]. In order to better understand the activation mechanism of hAT_1, we combined hAT_1 and its CAM as a prototypic pair, in a temperature dependent photoaffinity labeling study to explore the conformational landscape of this peptidergic GPCR. Photoaffinity labeling is a useful tool for structure activity studies as well as for elucidating structural changes occurring upon activation [18–22]. Among the most common photoprobes, p-benzoyl-L-phenylalanine (Bpa) is very stable under normal light conditions, it to react mainly with chemically inert C–H bonds and it has a very high cross-linking efficiency [23]. Using this approach, we found that ^{125}I-[Sar^1, Bpa^8] AngII reacts with residues 293–294 of transmembrane domain 7 in native (WT) hAT_1 receptor [22]. Unfortunately, the use of Bpa-based photoprobes has led to variabilities in yields, of labeling patterns, as well as a biased specificity for methionine [24–27]. Nevertheless, the inherent selectivity of Bpa towards methionine has been used as an advantage in finding new ligand contact points [16,19,20,22]. This inherent selectivity led to the elaboration of the methionine proximity assay (MPA) which is an iterative Met mutagenesis strategy on the receptor to explore new ligand contact points arising from inserting a methionine in the ligand binding environment and photolabeling it with a Bpa containing ligand [21]. Using the MPA approach we have further defined the position of residues in the binding site of hAT_1 (WT and CAM).

Furthermore, there are certain advantages of performing photolabeling at controlled temperatures [25,28,29]. Conceptually, by controlling and varying the photolabeling temperature one should be able to modulate the conformational landscape or the extent of conformational fluctuations of hAT_1 both in its WT and CAM background. It is anticipated that the extent of conformational fluctuations will be proportional to the kinetic energy or the temperature of the system and that the accessibility of residues in the binding pocket may, consequently, display a temperature dependency. Such a variation in the accessibility of binding site residues could be a direct indicator of the extent of temperature induced conformational fluctuations and dynamical behavior of the receptor. With this in mind, we have exploited the Met mutants that defined the residues forming the binding site within hAT_1 (WT and CAM) [16,19,20] for the C-terminal amino acid of the ligand and photolabeled them using the ^{125}I-[Sar^1, Bpa^8] AngII analogue at various temperatures from −20 to 50 °C.

2. Materials and methods

2.1. Materials

Bovine serum albumin (BSA), bacitracin, diisopropyl ethylamine, soybean trypsin inhibitor, Tris–HCl, acrylamide, deoxycolate acid, dithiothreitol (DTT), tricine, ethylenediaminetetraacetic acid (EDTA), and CNBr were from Sigma–Aldrich (Oakville, ON, Canada). Acetonitrile, acetic acid, methylene chloride, methanol, isopropanol, 2-mercapto-ethanol, trifluoroacetic acid, $NaHCO_3$, NaCl, $MgCl_2$, $CaCl_2$, glycerol, and ethylene glycol were from Fisher Scientific (Oakville, ON, Canada). KCl was from Anachemia (Lachine, Qc, Canada). Na_2HPO_4, NaH_2PO_4, and Sodium dodecyl sulfate (SDS) were from J.T. Baker (Phillipsburg, NJ, USA). Iodo-Gen was from Pierce (Rockford, IL, USA). Na^{125}I was from PerkinElmer (Waltham, MA, USA). Penicillin/streptomycin supplemented with L-glutamine and Tripsin were from Wisent (St-Bruno, Qc, Canada). Cell culture mediums were from Invitrogen (San Diego, CA, USA). FuGene 6 transfection reagent, PNGaseF, Nonyl phenoxylpolyethoxylethanol (NP-40), glycine, Trisma Base, and Protease Inhibitor Cocktail® were from Roche Diagnostics (Mannheim, Germany). Ammonium persulfate (APS), bromophenol blue, and tetramethylethylenediamine (TEMED) were from Bio-Rad (Mississauga, ON, Canada). X-ray films (Kodak Biomax®MS, Rochester, NY, USA) with intensifying screens were from Fischer Scientific.

2.2. Synthesis and radioiodination of the photoligand

^{125}I-[Sar^1, Bpa^8]AngII was prepared according to Bosse et al. [30]. The peptide was iodinated (1500 ± 500 Ci/mmol) as previously described [19,31], except that an acetic acid buffer (pH 5.4) was used.

2.3. Cell cultures and transfection of COS-7 cells

COS-7 cells were grown in Dulbecco's modified Eagle's medium (DMEM) supplemented with 2 mM L-glutamine, 10% (v/v) fetal bovine serum, 100 IU/ml penicillin, and 100 μg/ml streptomycin. The cells were incubated at 37 °C in a 5% CO_2 atmosphere and were transfected with the indicated plasmids [16,19,20,22] at ∼70% confluence using the FuGene 6 transfection reagent according to the manufacturer's instructions. Thirty-six hours after the initiation of transfection, the cells were washed once with PBS (137 mM NaCl, 0.9 mM $MgCl_2$, 3.5 mM KCl, 0.9 mM $CaCl_2$, 8.7 mM Na_2HPO_4, and 3.5 mM NaH_2PO_4, pH 7.4) and immediately stored at −80 °C until used.

2.4. Photoaffinity labeling

Frozen transfected COS-7 cells were thawed for 1 min at 37 °C. The broken cells were then gently scraped, resuspended in 10 ml of washing buffer (25 mM Tris–HCl [pH 7.4], 100 mM NaCl, and 5 mM $MgCl_2$), and centrifuged (500 × *g* for 10 min at 4 °C). The pellet was dispersed in binding buffer (25 mM Tris–HCl [pH 7.4], 100 mM NaCl, 5 mM $MgCl_2$, and 0.1% [w/v] BSA). The broken cell suspension (1 mg of protein) was incubated for 60 min at room temperature in the presence of 3 nM ^{125}I-[Sar^1, Bpa^8] AngII. After centrifugation at 500 × *g*, the pelleted broken cells were washed once and resuspended in 0.5 ml of ice-cold washing buffer prepared for corresponding temperature (pH of 7.4), then irradiated for 60 min in a temperature-controlled photoreaction chamber (±2 °C) in 5 ml Pyrex eppendorf tubes (Fisher Scientific) immersed in cooling solution (equal parts water and ethylene glycol) within the spiral cage of the UV source (13 W Noma® Mini Spiral Black light, λ_{max} 365 nm, serial no. 52-5146-0, Trileaf Distribution, Toronto, ON, Canada). The photoreaction chamber was placed in a temperature-controlled MGW Lauda RC20 Brinkman refrigeration unit equipped with a B. Braun Thermomix II and six UV light sources. The photolabeled samples were centrifuged (2500 × *g* for 10 min at 4 °C) and the pellet was solubilized for 30 min at 4 °C in m-Ripa buffer (50 mM Tris–HCl [pH 8.0], 150 mM NaCl, 0.5% [w/v] deoxycholate, 0.1% [w/v] SDS, and 1% [v/v] Nonidet P-40) supplemented with a protease inhibitor cocktail (Complete EDTA-Free) from Roche (Laval, QC, Canada). The cell lysate was centrifuged (15,000 × *g* for 25 min at 4 °C) to remove insoluble material and the supernatant was stored at −20 °C until used.

2.5. Partial purification of the labeled complex

The solubilized photolabeled receptor complexes were diluted in an equal volume of 2× Laemmli buffer (120 mM Tris–HCl [pH 6.8], 20% [v/v] glycerol, 4% [w/v] SDS, 200 mM DTT, and 0.05% [w/v] bromophenol blue) and incubated for 60 min at 37 °C. SDS-PAGE was performed as previously described [32] using a 10% polyacrylamide preparative gel. The gel was first exposed to an X-ray film (autoradiogram) with an intensifying screen and the radioactive region was then cut into slices. The labeled receptor was passively eluted from the gel slices into fresh electrophoresis buffer (25 mM Trizma Base [pH 8.3], 250 mM glycine, and 0.1% [w/

v] SDS) for 2–3 days at 4 °C with gentle agitation as described elsewhere [33]. The eluate (~40 ml) was concentrated to a final volume of 100–250 μl using an Amicon-10 filter from Millipore (Bedford, MA, USA), lyophilized, and dissolved in water in preparation for CNBr digestion.

2.6. Deglycosylation

The partially purified photolabeled receptor (up to 10,000 cpm) was dissolved in 45 μl of the PNGase F reaction buffer (50 mM Tris–Base pH 8.0, 25 mM EDTA, 0.5% [w/v] NP-40, 0.1% [w/v] SDS, 1% [v/v] 2-mercapto-ethanol). Five units of PNGase F were added to each sample and the reaction was carried out at 37 °C for 18–24 h.

2.7. CNBr Digestion and migration

The partially purified photolabeled receptor (up to 3500 cpm) was diluted in a 3:5 mixture of 30% trifluoroacetic acid and 50 mg/ml [w/v] of CNBr in 100% acetonitrile. The 100 μl samples were incubated at room temperature in the dark for 18–24 h. Water (1 ml) was added to terminate the reaction. The samples were lyophilized and dissolved in Tris-tricine with 1× Laemmli buffer, loaded (3500 cpm) on 16.5% SDS-PAGE Tris-tricine running gels from Bio-Rad (Hercules, CA, USA). Photolabeled bands were revealed by autoradiography on X-ray films from Kodak Biomax (Rochester, NY, USA). ^{14}C-labeled low molecular weight protein markers from Amersham Biosciences (Baie d'Urfé, QC, Canada) were used to determine apparent molecular weights. Running conditions and staining procedures were performed according to the manufacturer's instructions.

2.8. Ratio quantification

Autoradiograms were scanned as a high resolution .TIFF file. Fragments sizes were quantified by intensity and size using Adobe® photoshop 7.0 (San Jose, CA, USA) using the magnetic lasso and Histogram function. Gels were also sliced according to autoradiogram overlap onto the gel to isolate fragments and quantified by γ-counting in a Wallac 1470 WIZARD™ Gamma Counter (PerkinElmer). Direct gel count and densitometric analysis had a correlation of 0.94 (see Figure S1, supplementary data). The accessibility ratios ($r_{X/TM7}$) were obtained from these quantifications which correspond to the integrated radioactive intensities of the Met specific fragments divided by the integrated radioactive intensities of the native fragments, where X designates the location of the mutated Met in hAT_1. All quantifications were done at least in triplicate and all gel quantification comprise of the average of at least 3 individual variably exposed autoradiograms. Quantified Data was analyzed using Graphpad Prizm 5 (LaJolla, CA, USA).

2.9. Molecular modeling

All calculations were performed using a Silicon Graphics Octane2 workstation (Silicon Graphics Inc., Mountain View, CA, USA). Molecular modeling of the hAT_1 receptor was performed using the INSIGHTII suite of programs (Homology, Discover and Biopolymer; Accelrys, San Diego, CA, USA). The molecular model of hAT_1 (GenBank™ accession no. P30556) was based on the rhodopsin structure (Protein Data Bank: 1U19) [34]. The strictly conserved residues between the hAT_1 receptor and rhodopsin were aligned in order to identify and assign the structurally conserved regions. No gaps were observed inside the TMs. The coordinates of the structurally conserved regions were then transferred to the sequence of hAT_1. Non-structurally conserved loop regions were constructed using the generate command in the Homology module. This procedure [35] generates loop conformations with minimal potential energies by iteratively sampling the φ and ψ angles. The disulfide bonds between extracellular loops 1 and 2, and between the N-terminal and extracellular loop 3 were then added to hAT_1. The potential energy of the model was minimized with Discover using the Amber force field [35,36]. The minimization protocol consisted of three steps. In the first step, the coordinates of all the heavy atoms were fixed. During the second step, only the coordinates of the backbone atoms were fixed. Finally, only the backbone atoms of the TMs were fixed during the final minimization step. The atoms of the N-terminus were left unrestrained throughout the protocol. Distances were calculated using INSIGHTII. Figures were prepared using PyMol v. 0.99rc6 (Shrödinger, NY, USA).

2.10. Generation of ligand–WT hAT_1 receptor complex model structure

The [Bpa^8] AngII ligand was constructed using Builder by adding the Bpa moiety to the position 8 of the AngII NMR structure [37]. The [Bpa^8] AngII molecule was placed between TM3, 6, and 7 as suggested by previous studies [19,20] and the present photolabeling results. It was positioned to accommodate, as much as possible, the restraints (photolabeled Met residues, see below) used for the minimization without interfering with receptor side-chains. The complex between hAT_1 and [Bpa^8] AngII (with the coulombic terms turned off) was modeled by applying distance restraints between the Cβ atoms of the photolabeled Met residues and the ketone oxygen of Bpa and using a simulated annealing protocol described elsewhere [38]. The usual distance restraint used to accommodate a photolabeling contact point in previous studies [16,19,20] was within the range of 7.5 Å between the ketone oxygen of Bpa and the Cβ atoms of the photolabeled Met residues. Since the results here are presented as a ratio (r or $r_{X/TM7}$) of photolabeling between a Met residue (where X corresponds to the Ballesteros–Weinstein nomenclature) and the residues of TM7 (where TM7 refers to the labeling of either 293 or 294), the distance restraints (d) were calculated using the formulas explained in Section 3.6 of the results obtained at 0 °C. The non-Met residues 293 and 294 which could not be quantified as a $r_{X/TM7}$ were given 7.5 Å distance constraint in both WT and N111G templates [22].

2.11. Generation of ligand–CAM hAT_1 receptor complex model structure

The complex between the [Bpa^8] AngII ligand and the constitutively active CAM (N111G) mutant receptor was modeled by mutating the N111 residue on the basal model (WT) to a glycine, applying the corresponding distance restraints obtained from the residues' $r_{X/TM7}$ and using the simulated annealing protocol [38].

3. Results

3.1. Previously obtained contact points

In addition to the labeling of 293 and 294, the MPA approach allowed for the concurrent labeling of Met residues also accessible to the ^{125}I-[Sar^1, Bpa^8] AngII ligand in the hAT_1 binding site. These residues with their corresponding Ballesteros and Weinstein nomenclature [39,40], are F77M (2.53), L112M (3.36), Y113M (3.37), N200M (5.43), F249M (6.44), W253M (6.48), H256M (6.51), and T260M (6.55) [16,19,20]. This concurrent labeling is revisited and quantified below by precisely controlling the temperature of photolysis in both the WT and CAM hAT_1 receptors.

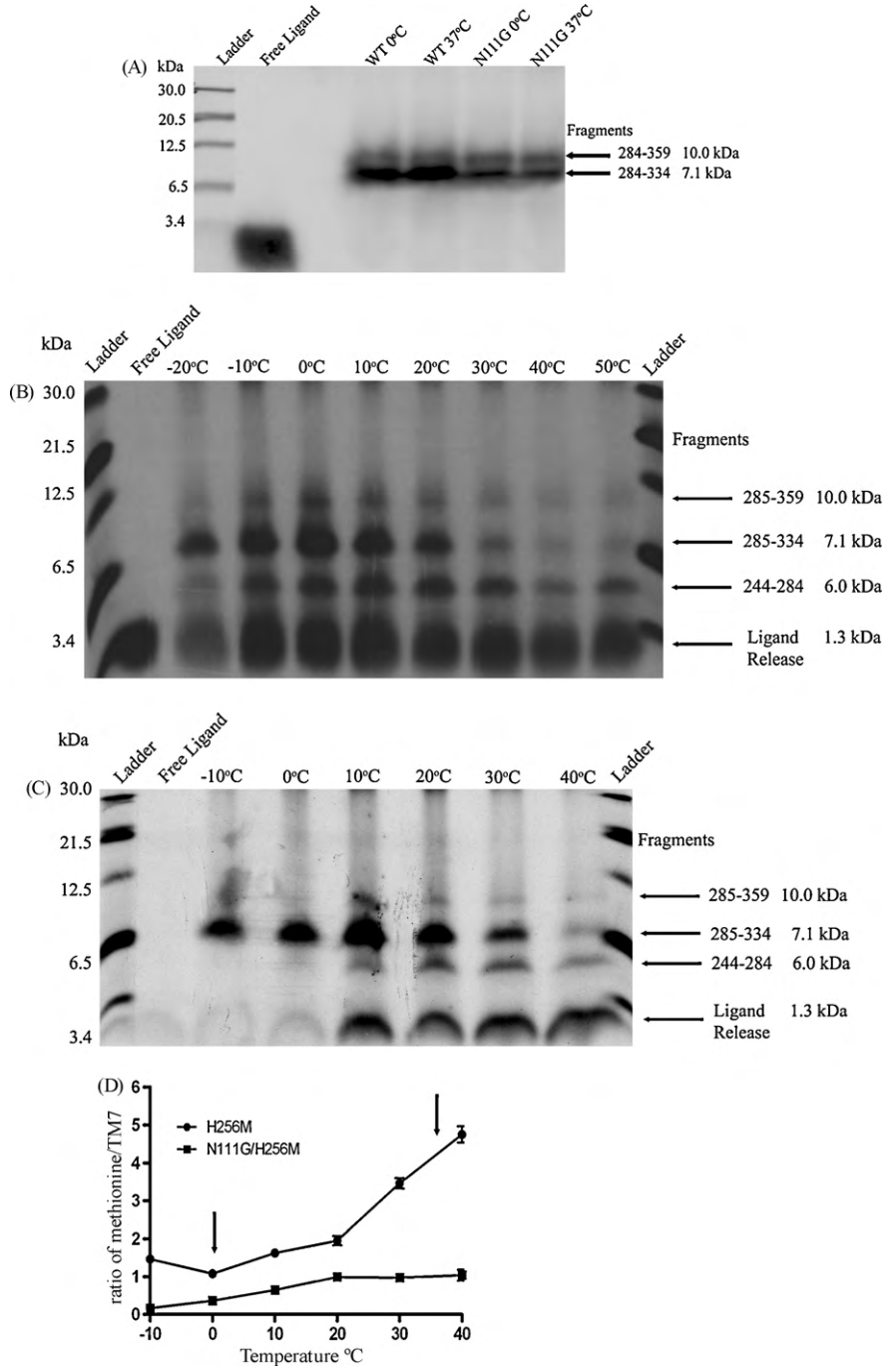

Fig. 1. Temperature dependent photolabeling of hAT_1. CNBr digestions of prepurified receptors followed by a 16.5% Tris-tricine SDS-PAGE and autoradiogramme. ^{125}I-[Sar^1, Bpa^8] was migrated alone in lane Free Ligand. (A) Photolabeling of WT and N111G hAT_1 at 0 and 37 °C gave identical fragmentation patterns for both mutants at different temperatures. (B and C) Photolabeling of H256M (panel B) and N111G/H256M (panel C) from −20 to 50 °C with ^{125}I-[Sar^1, Bpa^8]. (D) Quantification of photolabeling regions of H256M and N111G/H256M according to temperature. The signal which corresponds to TM6 labeling was divided by the signal which corresponds to TM7. Results are presented ± S.D. The H256M mutant was significantly more accessible at all temperatures than N111G/H256M ($p < 0.02$, $n = 3$). The arrows indicate the chosen temperatures for the subsequent analysis. Supplementary Figure 2 shows the quantification of WT and N111G hAT_1 labeling fragments.

3.2. Photolabeling of WT and CAM hAT_1 receptors at different temperatures

As a reference point, hAT_1 and N111G hAT_1 were photolabeled at 0 and at 37 °C (Fig. 1A). As previously observed, CNBr digestion of the prepurified receptors yields two characteristic fragments; a 10.0 kDa fragment corresponding to residues 285–359 (8.7 kDa) of TM7 and C-terminal tail in addition to the covalently attached ^{125}I-[Sar^1, Bpa^8] AngII (1.3 kDa) as well as the 7.1 kDa fragment corresponding to residues 285–334 (5.8 kDa) of TM7 in addition to ^{125}I-[Sar^1, Bpa^8] AngII (1.3 kDa). The 10.0 kDa fragment corresponds to an incomplete digestion at residue 333 M [19,22]. As described elsewhere, the Bpa moiety can attach to residues other than methionine, namely residues F293 and N294 [21,22]. There is no significant ligand release from CNBr digestion in Fig. 1A. This means that when no Met residues are engineered in either the WT

or the CAM, no endogenous Met side-chains are labeled. In the rest of the text, labeling at residue 293 or 294 will be referred to as TM7 labeling.

3.3. Photolabeling of H256M and N111G/H256M hAT$_1$ receptors at different temperatures

In order to assess the extent of the effect of temperature on the labeling of specific methionines, we have photolabeled the H256M hAT$_1$ (6.51) mutant with the [Sar^1, Bpa^8] AngII ligand at 10° increments from −20 to 50 °C (Fig. 1B). This mutant has been previously shown to have a temperature dependent shift in labeling patterns [25]. As can be seen there is a stark change in the labeled fragment proportions as a function of temperature. A loss of the 10.0 and 7.1 kDa fragments, representing non-Met labeling in TM7, is observed in favor of fragments at 6.0 and 1.3 kDa, respectively [25]. The new fragments correspond to residues 244–284 (4.7 kDa) of TM6 in addition to ^{125}I-[Sar^1, Bpa^8] AngII (1.3 kDa) while the second 1.3 kDa fragment corresponds to the CNBr induced ligand release (^{125}I-[Sar^1, Bpa^8] AngII-isothiocyanate). According to previous investigations, the Bpa moiety can covalently bind to either side of the Met-thioether, i.e. to carbon γ or ε on the methionine side-chain [19,22]. This will affect the CNBr digestions in two ways [19,21]. Firstly, labeling of Cγ methylene prevents cleavage at this methionine [19,22] and a new fragment, in this case, the 6.0 kDa fragment is observed. Secondly, if Bpa labels the distal Cε methyl group the CNBr digestion will cleave the peptide bond and the intermediate thiolactone formation will release the isothiocyanate-modified ligand [19,22]. This fragmentation pattern is only observable if a methionine is labeled.

The appearance of these new CNBr digestion fragments is a resultant of the fact that the Met at position 256 is in close proximity to the Bpa moiety in the ^{125}I-[Sar^1, Bpa^8] AngII-H256M hAT$_1$ complex. Moreover, the relative intensities of the two labeling patterns provide us with an indication of the relative accessibility of the Bpa moiety to the methionine relative to TM7 labeling. As discussed in more detail below, these intensities (methionine specific versus TM7 labeling) can be transformed into distances between the BPA and the mutated methionine and can serve as structural restraints in molecular modeling. Finally, changes in these relative intensities could potentially serve as an indication of a structural change in hAT$_1$ either as a function of temperature or constitutive activity.

Overall, the data presented in Fig. 1B, reveals as a function of increasing temperature, that the ^{125}I-[Sar^1, Bpa^8] AngII labels more efficiently the introduced methionine. This suggests that the input of energy into the system is translated into larger fluctuations in the ^{125}I-[Sar^1, Bpa^8] AngII-H256M hAT$_1$ complex [17,25].

With the aim to explore the potential effect of the CAM mutation on the digestion pattern observed above, we proceeded to the photolabeling of the N111G/H256M double mutant in function of the temperature of photolysis. The N111G/H256M hAT$_1$ as well as all the other Met mutants in the N111G background studied here retain constitutive activity (data not shown) indicating that the mutations do not impede the constitutive activation [16,20]. Furthermore, the ^{125}I-[Sar^1, Bpa^8] AngII has been shown to be a neutral agonist (or weak partial agonist) on the WT and CAM receptors which should not affect the active receptor populations [20]. Non-canonical activation pathways [12] for this ligand were not investigated in the previous studies [16,19–22]. Fig. 1C shows a temperature dependent shift on N111G/H256M hAT$_1$; it is similar to that observed on H256M hAT$_1$, but less pronounced. Higher temperatures are necessary to efficiently bring the BPA moiety closer to the methionine in the N111G/H256M hAT$_1$ receptor compared to the H256M hAT$_1$ receptor.

In order to quantify this shift, we have devised a ratio called the labeling accessibility ratio ($r_{X/TM7}$). This ratio is defined as the sum of the radioactivities of the Met specific fragments divided by the sum of the radioactivities of the "native" TM7 fragments, where *X* designates the position in the hAT$_1$ receptor where the introduced Met is located (Ballesteros–Weinstein nomenclature). Fig. 1D shows the $r_{6.51/TM7}$ of H256M hAT$_1$ and N111G/H256M hAT$_1$ as a function of temperature. At all temperatures, residue 256 had a higher $r_{6.51/TM7}$ in the WT background than in the CAM background ($p < 0.02$, $n = 3$). However, the accessibility of residue 256 in the CAM background increases less radically as indicated by the lower $r_{6.51/TM7}$. This suggests that conformational variations (compared to the WT background) may be caused by the CAM mutation present in the N111G/H256M hAT$_1$ receptor, which contributes to modulate the $r_{6.51/TM7}$ at the corresponding temperatures.

3.4. Photolabeling of TM2, 3, 5, and 6

As mentioned in Section 3.1, TM2 has only one MPA positive residue at position 77 (2.53). Compared to the native labeling, CNBr digestion of the photolabeled TM2 Met mutants yields a new fragment at 4.3 kDa corresponding to the residues 58–90 (3 kDa) plus ^{125}I-[Sar^1, Bpa^8] AngII (1.3 kDa) (see supplementary Figure 3A) [19]. Fig. 2A shows the $r_{2.53/TM7}$ ratios of both mutants. The

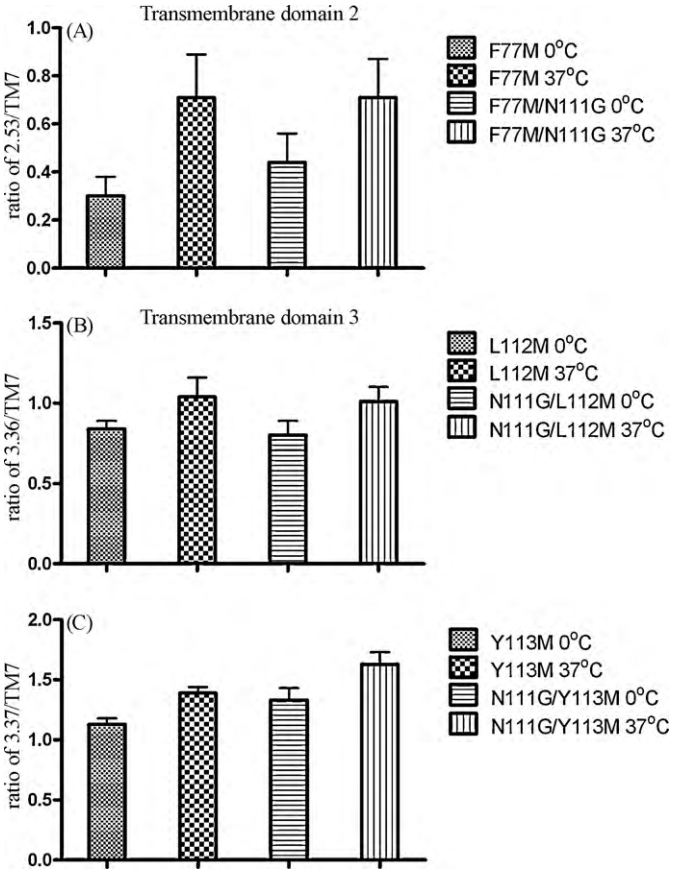

Fig. 2. Histograms of TM2 and 3. The signal which corresponds to TM2 or 3 was divided by the signal which corresponds to TM7 labeling. Results are presented ±S.D. (A) Quantification of photolabeling regions of F77M and F77M/N111G hAT$_1$ at 0 and 37 °C. The 37 °C photolabeling ratios was significantly more accessible than the 0 °C photolabeling ratios ($p < 0.05$, $n = 3$). (B) Quantification of photolabeling regions of L112M and N111G/L112M hAT$_1$ at 0 and 37 °C. The 37 °C photolabeling ratios was significantly more accessible than the 0 °C photolabeling ratios ($p < 0.01$, $n = 4$). (C) Quantification of photolabeling regions of Y113M and N111G/Y113M hAT$_1$ at 0 and 37 °C. The 37 °C photolabeling ratios was significantly more accessible than the 0 °C photolabeling ratios ($p < 0.01$, $n = 4$). This CAM variant was also significantly more accessible than the WT variants at both corresponding temperatures ($p < 0.01$, $n = 4$).

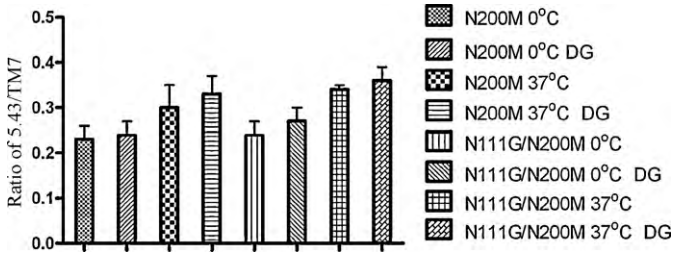

Fig. 3. Histogram of TM5. Quantification of photolabeling regions of N200M and N111G/N200M hAT_1 at 0 and 37 °C with or without deglycosylation (DG). The signal which corresponds to TM5 was divided by the signal which corresponds to TM7 labeling. Results are presented ±S.D. The 37 °C photolabeling ratios of N111G/N200M was significantly more accessible than the 0 °C photolabeling ratios ($p < 0.01$, $n = 3$).

F77M (2.53) mutants displayed a significant increase in photolabeling ratios at 37 °C compared to 0 °C in the WT and CAM backgrounds ($p < 0.05$, $n = 3$). There was no significant difference between the WT and CAM mutants regarding to the $r_{2.53/TM7}$ at a 95% confidence interval.

TM3 has two positive MPA residues; L112M (3.36) and Y113M (3.37). As previously determined, CNBr digestion of the photolabeled TM3 Met mutants yields a new fragment at 6.3 kDa which corresponds to residues 91–134 (5.0 kDa) plus ^{125}I-[Sar^1, Bpa^8] AngII (1.3 kDa) (see supplementary Figure 3B) [19]. Fig. 2B shows the $r_{3.36/TM7}$ for both receptor mutants. As observed above, the L112M (3.36) mutants displayed a significant increase in photolabeling ratios at 37 °C compared to 0 °C in the WT and CAM backgrounds ($p < 0.01$, $n = 4$). Again, there was no significant difference in photolabeling ratios. However, photolabeling of the other TM3 mutant, Y113M (3.37) (Supplementary Figure 3C) yields the same CNBr digestion patterns as L112M but with a slightly higher labeling accessibility ratio under all test conditions (Fig. 2C). It showed a significant increase in the $r_{3.37/TM7}$ in the constitutively active variant compared to WT background at both temperatures ($p < 0.01$, $n = 4$). This mutant also showed a significant increase in the $r_{3.37/TM7}$ at 37 °C when compared to 0 °C in both the WT and the CAM templates ($p < 0.01$, $n = 4$).

As stated in Section 3.1, TM5 has only one MPA positive position; N200M (5.43). CNBr digestion of the photolabeled Met mutant of TM5 yields a new fragment at 12.7 kDa which corresponds to the non-glycosylated fragment 142–243 (11.4 kDa) plus ^{125}I-[Sar^1, Bpa^8] AngII (1.3 kDa) (see supplementary Figure 3D) [16]. The residues 142–243 contain 2 N-glycosylation sites. Each of these glycosylations should cause an apparent increase in apparent mass of more than 20 kDa in the SDS-PAGE migrations [41,42]. However, enzymatic deglycosylation of these mutants did not significantly increase the N200M Cγ labeling fragment. This suggests that hAT_1 can be deglycosylated under the acidic conditions of CNBr digestion [43]. As seen in Fig. 3 the $r_{5.43/TM7}$ showed a significant temperature dependent increase for the CAM mutants only ($p < 0.01$). There was no observable increase in the $r_{5.43/TM7}$ of the WT versus CAM background.

In addition to H256M (6.51), TM6 has three additional MPA positive positions: 249 (6.44), 253 (6.48), and 260 (6.55). In comparison to the MPA positive positions found in the other TMs, these positions in TM6 showed the largest shift in labeling patterns. CNBr digestion of all the photolabeled TM6 mutants yields a fragment at 6.0 kDa (see above) which corresponds to the fragment 244–284 (4.7 kDa) in addition to ^{125}I-[Sar^1, Bpa^8] AngII (1.3 kDa) (see supplementary Figure 4). Fig. 4A shows the $r_{6.44/TM7}$ for this position. Again, the F249M (6.44) mutants displayed a significant increase in photolabeling ratios at 37 °C compared to 0 °C ($p < 0.001$, $n = 4$). There was also a significant decrease in labeling $r_{6.44/TM7}$ in the CAM background at both temperatures ($p < 0.001$, $n = 4$). A similar decrease is observable in the other TM6 mutants. Fig. 4B shows the $r_{6.48/TM7}$ for this position. A more significant decrease in the CAM background ($p < 0.0001$, $n = 4$) is observed as well as an increase in the $r_{6.48/TM7}$ at 37 °C compared to 0 °C ($p < 0.005$). Similarly, Fig. 4C shows the $r_{6.51/TM7}$ for this position. A significant decrease in the $r_{6.51/TM7}$ of the CAM backgrounds ($p < 0.005$, $n = 4$) is observed as well as an important increase in the $r_{6.51/TM7}$ at 37 °C compared to 0 °C ($p < 0.0001$). Finally, Fig. 4D shows the $r_{6.55/TM7}$ for this position. A significant

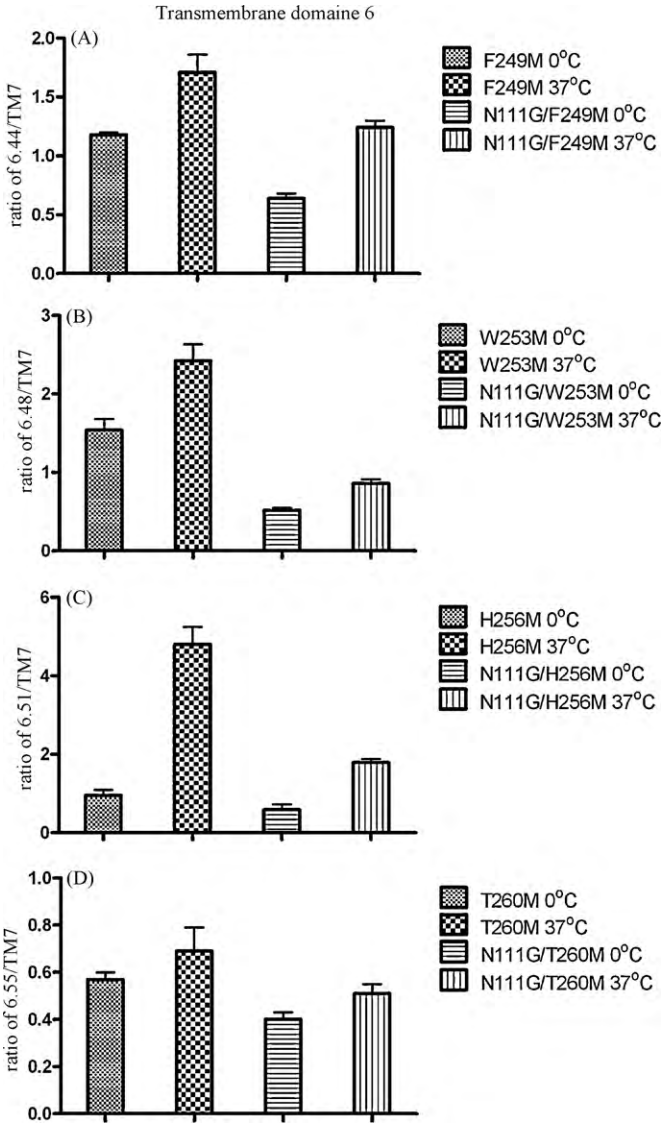

Fig. 4. Histograms of TM6. The signal which corresponds to TM6 labeling was divided by the signal which corresponds to TM7. Results are presented ±S.D. (A) Quantification of photolabeling regions of F249M and N111G/F249M hAT_1 at 0 and 37 °C. The 37 °C photolabeling ratios was significantly more accessible than the 0 °C photolabeling ratios ($p < 0.001$, $n = 4$). The CAM variant was significantly less accessible than the WT variants at both corresponding temperatures ($p < 0.001$, $n = 4$). (B) Quantification of photolabeling regions of W253M and N111G/W253M hAT_1 at 0 and 37 °C. The 37 °C photolabeling ratios was significantly more accessible than the 0 °C photolabeling ratios ($p < 0.005$, $n = 4$). The CAM variant was significantly less accessible than the WT variants at both corresponding temperatures ($p < 0.0001$, $n = 4$). (C) Quantification of photolabeling regions of H256M and N111G/H256M hAT_1 at 0 and 37 °C. The 37 °C photolabeling ratios was significantly more accessible than the 0 °C photolabeling ratios ($p < 0.0001$, $n = 4$). The CAM variant was significantly less accessible than the WT variants at both corresponding temperatures ($p < 0.005$, $n = 4$). (D) Quantification of photolabeling regions of T260M and N111G/T260M hAT_1 at 0 and 37 °C. The 37 °C photolabeling ratios was significantly more accessible than the 0 °C photolabeling ratios ($p < 0.05$, $n = 3$). The CAM variant was significantly less accessible than the WT variants at both corresponding temperatures ($p < 0.02$, $n = 3$).

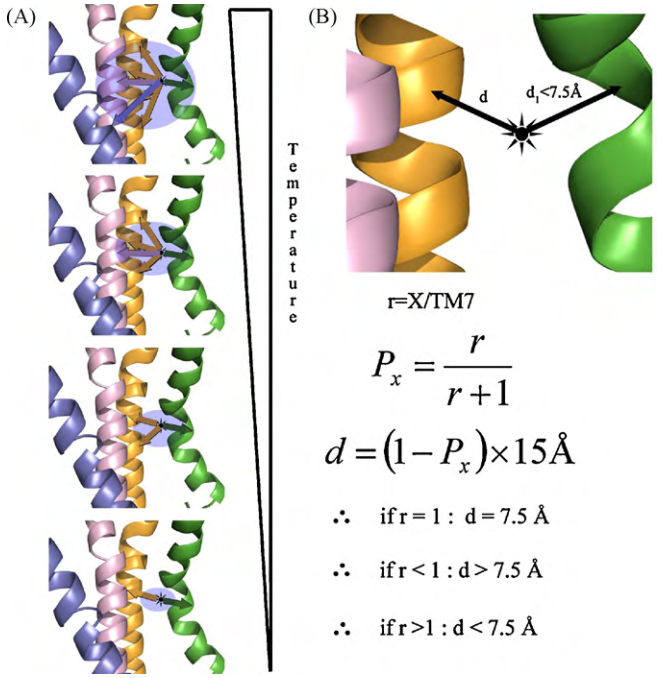

Fig. 5. The range of action of Bpa. Panel A shows a temperature dependent increase in the range of action (blue sphere) of the Bpa moiety (black star) inside the receptor. The higher range in action due to higher temperatures of photolysis, permit the labeling of more distant residues (colored lines) in different TMs. Panel B shows the formula for calculating distances (d) inside the receptor. If a given d_1 is up to 7.5 Å ($d_1 < 7.5$ Å) between the Bpa and the native TM7 residues, high $r_{X/TM7}$ would translate to a smaller d and conversely a lower $r_{X/TM7}$ would translate to a higher d between the Bpa moiety and the measured residue. Note that extremely high and extremely low $r_{X/TM7}$ would not be applicable with this formula.

decrease in the CAM background ($p < 0.02$, $n = 4$) is observed as well as an increase in the $r_{6.55/TM7}$ at 37 °C compared to 0 °C ($p < 0.05$).

3.5. Temperature and activation dependent changes in the $r_{X/TM7}$

Overall, the data presented above show that in all cases the $r_{X/TM7}$ increases as a function of temperature irrespective of the background (i.e. WT and CAM). This indicates that the inserted Met side-chains become increasingly accessible to the photolabile moiety as temperature rises. This is in complete agreement with increased amplitude of motions within the complex at higher temperature (see Fig. 5A). On the other hand, the $r_{X/TM7}$ of all TM6 MPA positive positions decreased in the CAM background. Conversely $r_{3.37/TM7}$ at position 113 was observed to increase in the CAM background. However, no significant change was observed between the backgrounds for the $r_{X/TM7}$ of the other mutants. Table 1 summarizes the $r_{X/TM7}$ of all mutants (see also supplementary Figure 5).

3.6. Converting the $r_{X/TM7}$ into distance constraints

Intuitively, conformational changes between the WT and the CAM complex are underlying these TM specific photolabeling variations. In order to characterize these underlying conformational changes, an empirical method to transform the $r_{X/TM7}$ into relative distances between the keto group of position 8 in ^{125}I-[Sar^1, Bpa^8] AngII and the two respective labeling loci (one in TM7 and the other on the Met mutated residue) is proposed. A high $r_{X/TM7}$ indicates that the labeling moiety is closer to the introduced Met than to positions 293 and 294 in TM7 and vice versa. The labeling radius of Bpa was estimated to be within 7.5 Å in a static model [16,19,22]. Hence, the maximal distance between two labeling sites could therefore amount up to 15 Å (Fig. 5B). For example, a ratio of 1 would indicate that there is no observed preference for either site. In this case the mutated Met residue would be given a distance restraint of 7.5 Å from the Bpa. In a case where the ratio is <1 there is a higher probability for the Bpa to be closer to 293 and 294 in TM7 and the average distance (in terms of a labeled population) from the introduced Met is expected to be larger than 7.5 Å. Inversely, for ratios greater than 1, the average distance from the Met should therefore be smaller than 7.5 Å. In order to estimate such a distance, we define below a function for determining the population of labeled Met mutation (P_X) as:

$$P_X = \frac{r}{r+1}$$

where r is the $r_{X/TM7}$ measured. Using this functional form and the measured ratios listed in Table 1 at low temperature one can calculate that P_X is comprised between 0.19 ($r_{X/TM7}$ = 0.23) and 0.6 ($r_{X/TM7}$ = 1.54). Hence, we propose to use the following equation to estimate the distance of Bpa from the Met of each MPA contact point:

$$d = (1 - P_X) \times 15\,Å$$

Table 1
The methionine/TM7 ratios ($r_{X/TM7}$) at 0 and 37 °C.

hAT$_1$ receptor	Ballesteros[a]	$r_{X/TM7}$ 0 °C			Distance restraint[b] to Bpa (Å)	$r_{X/TM7}$ 37 °C		
		Mean	±S.D.	N		Mean	±S.D.	N
F77M	2.53	0.3	0.08	3	11.6	0.71	0.18	3
F77M/N111G	2.53/3.35	0.44	0.12	3	10.4	0.71	0.16	3
L112M	3.36	0.84	0.05	4	8.2	1.04	0.12	4
N111G/L112M	3.35/3.36	0.8	0.09	4	8.3	1.01	0.09	4
Y113M	3.37	1.13	0.05	4	7.1	1.39	0.05	4
N111G/Y113M	3.35/3.37	1.33	0.1	4	6.4	1.63	0.1	4
N200M	5.43	0.23	0.03	3	12.2	0.3	0.05	3
N111G/N200M	3.35/5.43	0.24	0.03	3	12.1	0.34	0.01	3
F249M	6.44	1.18	0.02	4	6.9	1.71	0.15	4
N111G/F249M	3.35/6.44	0.64	0.04	4	9.1	1.24	0.06	4
W253M	6.48	1.54	0.14	4	5.9	2.42	0.21	4
N111G/W253M	3.35/6.48	0.52	0.03	4	9.9	0.86	0.05	4
H256M	6.51	0.96	0.13	4	7.7	4.8	0.44	4
N111G/H256M	3.35/6.51	0.59	0.14	4	9.4	1.79	0.08	4
T260M	6.55	0.57	0.03	4	9.6	0.69	0.1	4
N111G/T260M	3.35/6.55	0.4	0.03	4	10.7	0.51	0.04	4

[a] All mutants are shown with the Ballesteros and Weinstein nomenclature.
[b] The ratios at 0 °C were converted to relative distances (see Section 3.6). These were used in a simulated annealing protocol as the relative distance of the Bpa of ^{125}I-[Sar^1, Bpa^8] AngII and mutated Met residue.

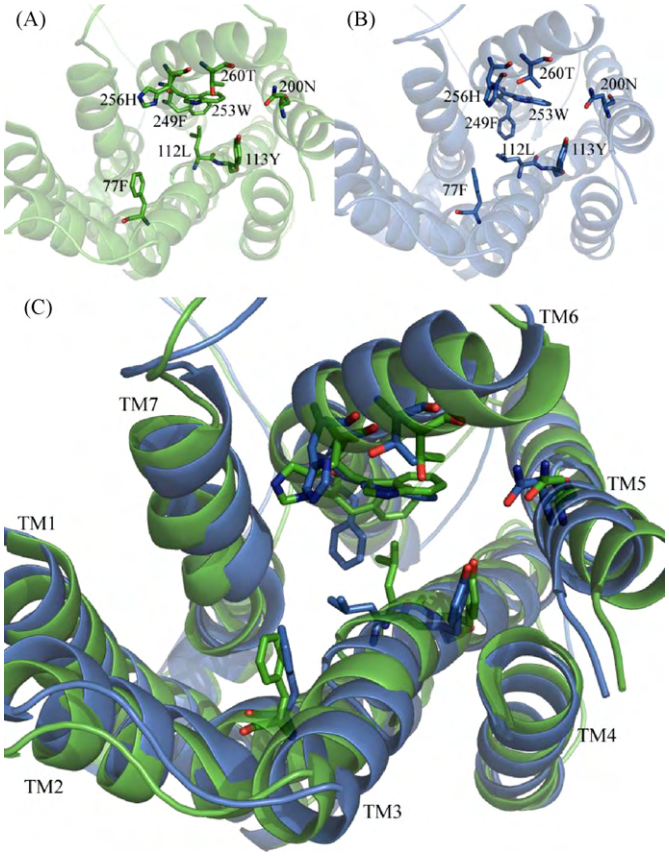

Fig. 6. Molecular modeling of WT and CAM hAT_1 using the distance constraints indicated in Table 1. The figures are shown from the extracellular perspective without the extracellular loops. (A) WT hAT_1 (Green). (B) CAM hAT_1 (Blue). (C) The overlap of both conformations. The ligand contact residues and TMs are indicated in black.

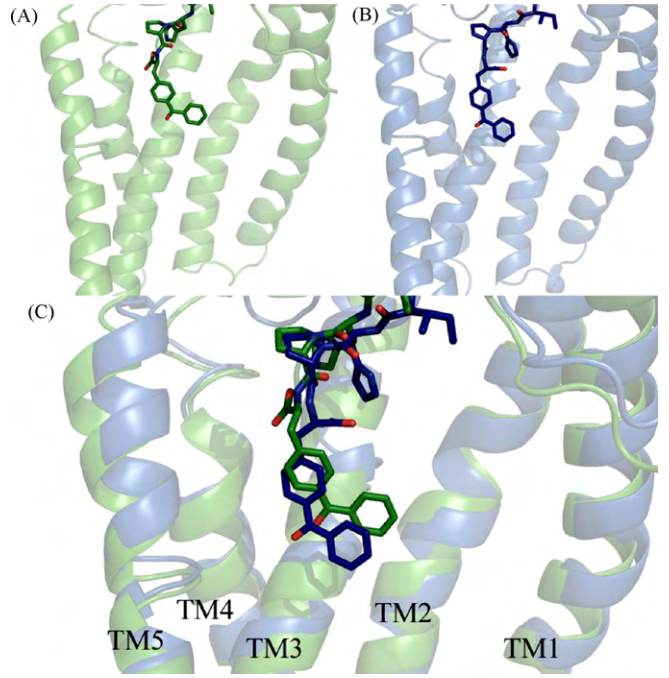

Fig. 7. Molecular modeling of WT and CAM hAT_1 using the distance constraints indicated in Table 1. The figures are shown from the membrane perspective through TM6 and 7 (up is the extracellular side and down is the intracellular side). (A) WT hAT_1 (Green). (B) CAM hAT_1 (Blue). (C) The overlap of both conformations.

Note that these distances represent the approximate position of the Bpa in the most abundantly labeled species and must only be taken as indicative of the most abundant state(s) of the complex. In order to limit the potential degeneration of these states, due to amplified fluctuation in the higher temperature complexes (methionines become increasingly labeled at higher temperatures) and optimally exploit the background specific information of the $r_{X/TM7}$, we will focus on the relative distances obtained from the 0 °C photolabeling in order to characterize potential conformational changes.

3.7. Characterization of the apparent conformational change between the WT and CAM hAT_1 by restrained simulated annealing

In order to evidence the measured conformational change between the WT and the CAM, we have used a simulated annealing approach [38] on homology models of both complexes (see Section 2). The distances are obtained at low temperature (Table 1) from the $r_{X/TM7}$ for each residue on both backgrounds and the differences between WT and CAM hAT_1 are shown in Fig. 6. The left panel displays the model for the WT hAT_1, the right panel depicts the CAM hAT_1 and the lower panel shows their superposition. An apparent displacement of TM3, an outward movement of TM6, and an inward movement of TM2 and 5 are visible. Analysis of the ligand position in the CAM background reveals a slight shift towards the intracellular side compared to WT hAT_1 (Fig. 7).

4. Discussion

The elucidation of conformational changes between the active and inactive forms of GPCRs has been a daunting task so far. The present contribution applies an extension of the photoaffinity labeling approach to evidence conformational changes in the receptor core that are associated with receptor activation. The extracellular and intracellular domains were therefore not addressed in the present study. Intermolecular distances were estimated from relative labeling yields (Fig. 5) and those distances were used in a simulated annealing protocol to generate models for both the WT and the CAM–hAT_1 complexes with a photoligand: ^{125}I-[Sar^1, Bpa^8] AngII. Using such an approach, we have been able to unveil differences between the relative orientations of the TMs in the WT and the CAM complexes as depicted in Fig. 6. Although our results indicate that the N111G hAT_1 mutant can adopt a different conformation than the WT receptor in the presence of ^{125}I-[Sar^1, Bpa^8] AngII, it is impossible, at this stage, to ascertain that the differential labeling in the CAM describes a 100% population of the receptor in a fully active state that couples to $G_{q/11}$. Indeed, the labeling could either describe a 100% population of partially active receptor or a population of less 100% of fully active receptors. However, and as described below, the relative movements of the TMs we unveiled are reminiscent of those reported for the activation of bRho. Moreover, our findings are also supported by results obtained with other biochemical methods on hAT_1 (e.g. SCAM, see below) and its N111G CAM and on other GPCRs in the rhodopsin family. Hence it appears that the movements of the TMs reported here for hAT_1 may prove, in the future, to be somewhat general in the activation mechanism of GPCRs of the rhodopsin family.

The Substituted Cystein Accessibility Method (SCAM) on all TMs of hAT_1 and its CAM was recently completed. The SCAM studies on TM2, which uses the cationic methanethiosulfonate-ethylammonium (MTSEA) to interfere with [Sar^1, Ile^8] AngII binding, suggests an integral pivot of TM2 towards the binding pocket in the CAM receptor [44]. A similar displacement is also apparent in Fig. 6. The SCAM study on TM3 suggested a counterclockwise rotation of TM3 in hAT_1 [45]. Here, position

113 (3.37) shows a significant increase in $r_{3.37/TM7}$ in the CAM template, which suggests a displacement of this residue towards the ligand binding environment. This translated into a slight movement of TM3 in our CAM complex model (Fig. 6). In accordance with the results of the SCAM study on TM5 [46], a slight movement of this TM towards the binding pocket in the CAM complex model is also noticeable (Fig. 6). Finally, the apparent outward displacement of TM6 (Fig. 6), was suggested by a very significant decrease in the $r_{X/TM7}$ of 4 contact points in the CAM background; this is also supported by the results of the SCAM study on TM6 [47]. Similarly, in a SCAM study on WT and CAM β2-adrenergic receptors, TM6 was also shown to move away from TM3 [48].

The best documented case of GPCR activation comes from the structural studies on the opsin family for which numerous crystallographic structures are known. These results indicate that TM6 is moving away from the retinal binding pocket while TM2, 5 and 7 move closer to it upon activation [49,50]. A slight displacement of TM3 is also reported [49–52]. Our findings on WT and CAM hAT_1 show almost identical displacements. We demonstrate that the ligand binds very closely to residue W253M (6.48) in the WT background and that this interaction is diminished in the CAM background. Residue 6.48 has been shown to be important for agonist activation and it is known as the "toggle switch" in TM6 [48,50]. In the CAM model the ligand binds deeper inside the transmembrane core which might be necessary for G protein activation (Fig. 7). A similar observation has been reported in the bRho by molecular dynamics simulations which showed a wider retinal binding cleft in a more dynamic and flexible agonist-receptor complex [50]. Since it has been previously shown that position 8 of the AngII analogue ^{125}I-[Sar^1, Bpa^8] AngII interacts with the same environment as retinal in bRho these results further validate our approach and the ensuing results. Hence, the reported TM rearrangements indicate that hAT_1 and bRho undergo similar conformational changes which was seen in the comparison of bRho with its G protein bound opsin structure [3,49]. Whether these rearrangements represent a general feature of the activation of GPCRs from the Rhodopsin family remains to be demonstrated by similar studies on other receptors of this class.

Another goal of this study was to evaluate the effect of temperature on the conformational fluctuations of the complexes. We have shown that the $r_{X/TM7}$ or the methionine specific labeling is favored at higher temperature. This can be interpreted as an increase in the amplitude of temperature induced fluctuations that favor methionine labeling at the expense of "native", non-Met labeling at positions 293 and 294 in TM7. This leads to an apparently larger reaction radius of Bpa at higher temperatures (Fig. 5). Hence, the use of high temperatures for photolabeling may highlight constraints that are artificially biased by structural fluctuations. The obtained results show that precise temperature control during photolysis and the use of sub-physiological temperatures (e.g. 0–10 °C) are important to optimize the resolution of the data obtained from ligand contact points in a given GPCR. However, the use of physiological temperatures during photolabeling permits to explore the range of structurally accessible conformations in a physiologically relevant ligand–receptor interaction. A particular structural state relevant for signal transduction could easily be inaccessible at 0° C where normal signaling activity is mostly absent in homoeothermic organisms.

In conclusion, we have shown that distance restraints obtained from temperature-controlled MPA on hAT_1 can be used with a simulated annealing protocol to highlight conformational changes occurring upon receptor activation. This was exemplified by the comparison of the ^{125}I-[Sar^1, Bpa^8] AngII–WT hAT_1 complex to the ^{125}I-[Sar^1, Bpa^8] AngII–CAM hAT_1 complex. Further photoaffinity labeling studies of hAT_1 and its CAM using other photolabile AngII analogues are currently underway. The presented labeling strategy is generally applicable to any peptidergic GPCR and could permit access to highly pertinent structural and conformational information in absence of complete X-ray or NMR structures.

Acknowledgements

We would like to thank Marie-Reine Lefebvre and Dr. Brian J. Holleran for their invaluable support and expertise. This research was financed by the CIHR. Emanuel Escher is a recipient of the J.C. Edwards Chair in Cardiovascular Research. Pierre Lavigne is a Chercheur Boursier Sénior of the Fonds en Recherche de la Santé du Québec (FRSQ). Richard Leduc is a Chercheur National of the FRSQ. This article was submitted to fulfill the requirements of a Ph.D. thesis for Jason Arsenault at the Université de Sherbrooke.

Appendix A. Supplementary data

Supplementary data associated with this article can be found, in the online version, at doi:10.1016/j.bcp.2010.06.004.

References

[1] Cherezov V, Rosenbaum DM, Hanson MA, Rasmussen SG, Thian FS, Kobilka TS, et al. High-resolution crystal structure of an engineered human beta2-adrenergic G protein-coupled receptor. Science 2007;318:1258–65.
[2] Day PW, Rasmussen SG, Parnot C, Fung JJ, Masood A, Kobilka TS, et al. A monoclonal antibody for G protein-coupled receptor crystallography. Nat Methods 2007;4:927–9.
[3] Scheerer P, Park JH, Hildebrand PW, Kim YJ, Krauss N, Choe HW, et al. Crystal structure of opsin in its G-protein-interacting conformation. Nature 2008; 455:497–502.
[4] Cozzini P, Kellogg GE, Spyrakis F, Abraham DJ, Costantino G, Emerson A, et al. Target flexibility: an emerging consideration in drug discovery and design. J Med Chem 2008;51:6237–55.
[5] Kenakin T. Allosteric theory: taking therapeutic advantage of the malleable nature of GPCRs. Curr Neuropharmacol 2007;5:149–56.
[6] Leach K, Sexton PM, Christopoulos A. Allosteric GPCR modulators: taking advantage of permissive receptor pharmacology. Trends Pharmacol Sci 2007;28:382–9.
[7] May LT, Leach K, Sexton PM, Christopoulos A. Allosteric modulation of G protein-coupled receptors. Annu Rev Pharmacol Toxicol 2007;47:1–51.
[8] Vauquelin G, Van Liefde I. G protein-coupled receptors: a count of 1001 conformations. Fundam Clin Pharmacol 2005;19:45–56.
[9] Kobilka B, Schertler GF. New G-protein-coupled receptor crystal structures: insights and limitations. Trends Pharmacol Sci 2008;29:79–83.
[10] Urban JD, Clarke WP, von Zastrow M, Nichols DE, Kobilka B, Weinstein H, et al. Functional selectivity and classical concepts of quantitative pharmacology. J Pharmacol Exp Ther 2007;320:1–13.
[11] de Gasparo M, Catt KJ, Inagami T, Wright JW, Unger T. International union of pharmacology. XXIII. The angiotensin II receptors. Pharmacol Rev 2000;52: 415–72.
[12] Hunyady L, Catt KJ. Pleiotropic AT1 receptor signaling pathways mediating physiological and pathogenic actions of angiotensin II. Mol Endocrinol 2006;20:953–70.
[13] Kenakin T. Functional selectivity through protean and biased agonism: who steers the ship? Mol Pharmacol 2007;72:1393–401.
[14] Auger-Messier M, Clement M, Lanctot PM, Leclerc PC, Leduc R, Escher E, et al. The constitutively active N111G-AT1 receptor for angiotensin II maintains a high affinity conformation despite being uncoupled from its cognate G protein Gq/11alpha. Endocrinology 2003;144:5277–84.
[15] Nikiforovich GV, Mihalik B, Catt KJ, Marshall GR. Molecular mechanisms of constitutive activity: mutations at position 111 of the angiotensin AT1 receptor. J Pept Res 2005;66:236–48.
[16] Clement M, Cabana J, Holleran BJ, Leduc R, Guillemette G, Lavigne P, et al. Activation induces structural changes in the liganded angiotensin II type 1 receptor. J Biol Chem 2009;284:26603–12.
[17] Arsenault J, Renaud MP, Clement M, Fillion D, Guillemette G, Leduc R, et al. Temperature-induced ligand contact point variations of the hAT1 receptor and of the constitutively active mutant N111G-hAT1. Adv Exp Med Biol 2009;611:339–40.
[18] Ruoho AE, Kiefer H, Roeder PE, Singer SJ. The mechanism of photoaffinity labeling. Proc Natl Acad Sci USA 1973;70:2567–71.
[19] Clement M, Martin SS, Beaulieu ME, Chamberland C, Lavigne P, Leduc R, et al. Determining the environment of the ligand binding pocket of the human angiotensin II type I (hAT1) receptor using the methionine proximity assay. J Biol Chem 2005;280:27121–9.

[20] Clement M, Chamberland C, Perodin J, Leduc R, Guillemette G, Escher E. The active and the inactive form of the hAT1 receptor have an identical ligand-binding environment: an MPA study on a constitutively active angiotensin II receptor mutant. J Recept Signal Transduct Res 2006;26:417–33.
[21] Rihakova L, Deraet M, Auger-Messier M, Perodin J, Boucard AA, Guillemette G, et al. Methionine proximity assay, a novel method for exploring peptide ligand–receptor interaction. J Recept Signal Transduct Res 2002;22: 297–313.
[22] Perodin J, Deraet M, Auger-Messier M, Boucard AA, Rihakova L, Beaulieu ME, et al. Residues 293 and 294 are ligand contact points of the human angiotensin type 1 receptor. Biochemistry 2002;41:14348–56.
[23] Saviano M, Improta R, Benedetti E, Carrozzini B, Cascarano GL, Didierjean C, et al. Benzophenone photophore flexibility and proximity: molecular and crystal-state structure of a Bpa-containing trichogin dodecapeptide analogue. Chembiochem 2004;5:541–4.
[24] Marciniak B, Bobrowski K, Hug GL. Quenching of triplet states of aromatic ketones by sulfur-containing amino acids in solution. Evidence for electron transfer. J Am Chem Soc 1993;97:11937–43.
[25] Arsenault J, Renaud MP, Clement M, Fillion D, Guillemette G, Leduc R, et al. Temperature-dependent variations of ligand–receptor contact points in hAT(1). J Pept Sci 2007;13:575–80.
[26] Wittelsberger A, Thomas BE, Mierke DF, Rosenblatt M. Methionine acts as a "magnet" in photoaffinity crosslinking experiments. FEBS Lett 2006;580: 1872–6.
[27] Kawamura A, Hindi S, Mihai DM, James L, Aminova O. Binding is not enough: flexibility is needed for photocrosslinking of Lck kinase by benzophenone photoligands. Bioorg Med Chem 2008;16:8824–9.
[28] Souto ML, Borhan B, Nakanishi K. Low-temperature photoaffinity labeling of rhodopsin and intermediates along transduction path. Methods Enzymol 2000;316:425–35.
[29] Dong M, Miller LJ. Effects of pH and temperature on photoaffinity labeling of Family B G protein-coupled receptors. Regul Pept 2009;158:110–5.
[30] Bosse R, Servant G, Zhou LM, Boulay G, Guillemette G, Escher E. Sar1-p-benzoylphenylalanine-angiotensin, a new photoaffinity probe for selective labeling of the type 2 angiotensin receptor. Regul Pept 1993;44:215–23.
[31] Fraker PJ, Speck Jr JC. Protein and cell membrane iodinations with a sparingly soluble chloroamide, 1,3,4,6-tetrachloro-3a,6a-diphrenylglycoluril. Biochem Biophys Res Commun 1978;80:849–57.
[32] Laemmli UK. Cleavage of structural proteins during the assembly of the head of bacteriophage T4. Nature 1970;227:680–5.
[33] Blanton MP, Cohen JB. Identifying the lipid-protein interface of the Torpedo nicotinic acetylcholine receptor: secondary structure implications. Biochemistry 1994;33:2859–72.
[34] Okada T, Sugihara M, Bondar AN, Elstner M, Entel P, Buss V. The retinal conformation and its environment in rhodopsin in light of a new 2.2 A crystal structure. J Mol Biol 2004;342:571–83.
[35] Shenkin PS, Yarmush DL, Fine RM, Wang HJ, Levinthal C. Predicting antibody hypervariable loop conformation. I. Ensembles of random conformations for ringlike structures. Biopolymers 1987;26:2053–85.
[36] Cornell WD, Cieplak P, Bayly CI, Gould IR, Merz KM, Ferguson DM, et al. A second generation force field for the simulation of proteins, nucleic acids, and organic molecules (vol. 117, p. 5179, 1995). J Am Chem Soc 1996;118:2309.
[37] Spyroulias GA, Nikolakopoulou P, Tzakos A, Gerothanassis IP, Magafa V, Manessi-Zoupa E, et al. Comparison of the solution structures of angiotensin I & II. Implication for structure–function relationship. Eur J Biochem 2003;270:2163–73.
[38] Charest G, Lavigne P. Simple and versatile restraints for the accurate modeling of alpha-helical coiled-coil structures of multiple strandedness, orientation and composition. Biopolymers 2006;81:202–14.
[39] Ballesteros JA, Weinstein H. Integrated methods for the construction of three-dimensional models and computational probing of structure–function relations in G protein coupled receptors. Meth Neurosci 1995;25:366–428.
[40] Ballesteros JA, Shi L, Javitch JA. Structural mimicry in G protein-coupled receptors: implications of the high-resolution structure of rhodopsin for structure-function analysis of rhodopsin-like receptors. Mol Pharmacol 2001;60:1–19.
[41] Lanctot PM, Leclerc PC, Clement M, Auger-Messier M, Escher E, Leduc R, et al. Importance of N-glycosylation positioning for cell-surface expression, targeting, affinity and quality control of the human AT1 receptor. Biochem J 2005;390:367–76.
[42] Lanctot PM, Leclerc PC, Escher E, Leduc R, Guillemette G. Role of N-glycosylation in the expression and functional properties of human AT1 receptor. Biochemistry 1999;38:8621–7.
[43] Donald AS. Partial deglycosylation of blood-group-specific glycoproteins. Biochem J 1980;185:327–37.
[44] Domazet I, Holleran BJ, Martin SS, Lavigne P, Leduc R, Escher E, et al. The second transmembrane domain of the human type 1 angiotensin II receptor participates in the formation of the ligand binding pocket and undergoes integral pivoting movement during the process of receptor activation. J Biol Chem 2009;284:11922–9.
[45] Martin SS, Boucard AA, Clement M, Escher E, Leduc R, Guillemette G. Analysis of the third transmembrane domain of the human type 1 angiotensin II receptor by cysteine scanning mutagenesis. J Biol Chem 2004;279:51415–23.
[46] Domazet I, Martin SS, Holleran BJ, Morin ME, Lacasse P, Lavigne P, et al. The fifth transmembrane domain of angiotensin II Type 1 receptor participates in the formation of the ligand-binding pocket and undergoes a counterclockwise rotation upon receptor activation. J Biol Chem 2009;284:31953–61.
[47] Martin SS, Holleran BJ, Escher E, Guillemette G, Leduc R. Activation of the angiotensin II type 1 receptor leads to movement of the sixth transmembrane domain: analysis by the substituted cysteine accessibility method. Mol Pharmacol 2007;72:182–90.
[48] Shi L, Liapakis G, Xu R, Guarnieri F, Ballesteros JA, Javitch JA. Beta2 adrenergic receptor activation. Modulation of the proline kink in transmembrane 6 by a rotamer toggle switch. J Biol Chem 2002;277:40989–96.
[49] Ahuja S, Smith SO. Multiple switches in G protein-coupled receptor activation. Trends Pharmacol Sci 2009;30:494–502.
[50] Bhattacharya S, Hall SE, Vaidehi N. Agonist-induced conformational changes in bovine rhodopsin: insight into activation of G-protein-coupled receptors. J Mol Biol 2008;382:539–55.
[51] Salom D, Lodowski DT, Stenkamp RE, Le Trong I, Golczak M, Jastrzebska B, et al. Crystal structure of a photoactivated deprotonated intermediate of rhodopsin. Proc Natl Acad Sci USA 2006;103:16123–8.
[52] Park JH, Scheerer P, Hofmann KP, Choe HW, Ernst OP. Crystal structure of the ligand-free G-protein-coupled receptor opsin. Nature 2008;454:183–7.